



Unraveling driving forces explaining significant reduction in satellite-inferred Arctic surface albedo since the 1980s

Rudong Zhang^{a,1}, Hailong Wang^{a,1}, Qiang Fu^b, Philip J. Rasch^a, and Xuanji Wang^c

^aAtmospheric Sciences and Global Change Division, Pacific Northwest National Laboratory, Richland, WA 99352; ^bDepartment of Atmospheric Sciences, University of Washington, Seattle, WA 98195; and ^cCooperative Institute for Meteorological Satellite Studies/Space Science and Engineering Center, University of Wisconsin-Madison, Madison, WI 53706

Edited by V. Ramanathan, Scripps Institution of Oceanography, University of California San Diego, La Jolla, CA, and approved October 10, 2019 (received for review September 3, 2019)

The Arctic has warmed significantly since the early 1980s and much of this warming can be attributed to the surface albedo feedback. In this study, satellite observations reveal a 1.25 to 1.51% per decade absolute reduction in the Arctic mean surface albedo in spring and summer during 1982 to 2014. Results from a global model and reanalysis data are used to unravel the causes of this albedo reduction. We find that reductions of terrestrial snow cover, snow cover fraction over sea ice, and sea ice extent appear to contribute equally to the Arctic albedo decline. We show that the decrease in snow cover fraction is primarily driven by the increase in surface air temperature, followed by declining snowfall. Although the total precipitation has increased as the Arctic warms, Arctic snowfall is reduced substantially in all analyzed data sets. Light-absorbing soot in snow has been decreasing in past decades over the Arctic, indicating that soot heating has not been the driver of changes in the Arctic snow cover, ice cover, and surface albedo since the 1980s.

Arctic amplification | albedo reduction | snow cover | sea ice | soot

Since the 1980s, the Arctic region has warmed 2 to 3 times faster than the global mean (1, 2), a feature often called Arctic amplification (3). Instrumental data, proxy records, and climate models have documented this phenomenon across a range of timescales in the past climate, and it is also simulated by models in future projections (4–8). Here we analyze results from a global aerosol-climate model simulation with satellite, reanalysis, and field-research data to interpret these features of the climate record. We focus on the trends in surface albedo, snow cover fraction, temperature, snowfall, and soot deposition during the recent decades (1980 to 2014) in the Arctic (60 to 90°N).

As the Arctic warms (e.g., due to the increase of greenhouse gases and/or atmospheric circulation changes), the retreat of snow and ice together with the associated feedbacks is known to be an important reason for Arctic amplification of the warming (8–15). Reduction of surface snow and ice results in a decrease of surface albedo, allowing for more solar heating that further decreases the snow and ice area, commonly known as the surface albedo feedback. In addition, since snow and ice insulate the surface, their decrease can also increase sensible and latent heat fluxes to the atmosphere, further increasing the atmospheric temperature profile (8, 16). Satellite observations reveal a 1.4% per decade reduction in the Arctic annual-mean surface albedo from 1982 to 1999 (17) and a significant decreasing trend in annual snow duration over the Arctic land surface during 2001 to 2014 (18). A recent observational study (19) shows a positive trend in the annual-mean solar radiation absorbed over the Arctic ocean that is about twice the trend over the Arctic land during 1982 to 2015, presumably, due to differences in albedo reduction over land and ocean. However, little is known about the relative contributions in snow versus

sea ice cover to the observed albedo reduction. Precipitation is projected to increase in a warmer world (20), more so in the Arctic than the global mean (21, 22). This amplified increase in the Arctic has been attributed to an increase in surface evaporation associated with sea ice retreat, as well as increased poleward moisture transport from lower latitudes (23). Although total precipitation is expected to increase, snowfall may decrease, and rainfall may dominate (24). We find in this study that the increase in surface air temperature and decrease in snowfall appear to drive the decrease in snow cover fraction explaining about 70% of the observed reduction in Arctic surface albedo since the 1980s, while the sea ice retreat played a secondary role.

The albedo of sea ice ranges from 0.1 when it contains dark ponds to 0.7 for bare white ice (25). Snow has a higher albedo, typically 0.7 to 0.8 for aged snow and 0.8 to 0.9 for fresh snow (26). Therefore, snow on sea ice can change the surface albedo and affect ice melting. The albedo of snow and ice can also be reduced by the presence of light-absorbing impurities (27) such as soot from the incomplete combustion of fossil fuels, biofuels, and biomass (28). Research efforts to measure these impurities and quantify their effects on albedo (29–34) indicate that these

Significance

Changes in snow cover, sea ice cover, and surface albedo over the Arctic are important for local warming and midlatitude climate change. Here, multiple datasets are used to show that observed reductions in the Arctic surface albedo in recent decades are largely linked to the decrease in Arctic snow cover fraction. The reduced snow cover fraction, driven by surface warming and declining snowfall, explains 70% of the observed reduction in the Arctic surface albedo. While absorbing aerosol (soot) falling on snow and ice can also reduce the surface albedo, the amount of soot in snow has actually been decreasing in recent decades, so soot deposition does not appear to explain the decreasing trend in snow cover and surface albedo.

Author contributions: R.Z., H.W., and Q.F. designed research; R.Z. and H.W. performed research; R.Z. and X.W. analyzed AVHRR APP-x satellite data; and R.Z., H.W., Q.F., P.J.R., and X.W. wrote the paper.

The authors declare no competing interest.

This article is a PNAS Direct Submission.

This open access article is distributed under [Creative Commons Attribution-NonCommercial-NoDerivatives License 4.0 \(CC BY-NC-ND\)](#).

Data deposition: CAM5 model data are available at https://release.datahub.pnnl.gov/released_data/990.

¹To whom correspondence may be addressed. Email: rudong.zhang@pnnl.gov or hailong.wang@pnnl.gov.

This article contains supporting information online at www.pnas.org/lookup/suppl/doi:10.1073/pnas.1915258116/-DCSupplemental.

First published November 11, 2019.

absorbing particles can reduce snow albedo in the visible wavelengths. These signatures are evident in radiative transfer modeling (27) and experiments on artificial snow (31). It has been hypothesized that absorbing soot deposition on the snow and ice surface has contributed to the accelerated melting of Arctic sea ice and snow in recent decades (35). However, measured soot content in recent Arctic snow appears no higher than it was several decades ago (29, 30), which does not support that hypothesis. Although relevant measurements are sparse in the Arctic, the observed decreasing soot content is consistent with recent emission reductions (36) in major contributing source regions such as Europe and Russia (37). State-of-the-art climate models using consistently calibrated historical emission inventories (36, 38) can help in providing a coherent picture of Arctic soot trends and their impact on the surface albedo. Results below indicate that there is a relatively small impact by soot on the Arctic surface albedo in magnitude compared to the impact of declining snow cover fraction.

Results

Decreased Albedo. The Advanced Very High Resolution Radiometer (AVHRR) and the Clouds & Earth's Radiant Energy System (CERES) satellite data products have been widely used to investigate Arctic climate variability and trends (17, 39). We use versions of these satellite-based monthly mean surface and planetary (top of atmosphere) albedo data sets (*Materials and Methods*) to compare to and build confidence in the Community Atmosphere Model version 5 (CAM5) simulated changes over the Arctic, and then diagnose the model output to better understand the cause of simulated albedo changes. To compare the CAM5 results with satellite-based albedo, we use the mean albedo for the months from March to September. Mean surface albedo over the entire Arctic (60 to 90°N) is obtained using the surface downwelling shortwave flux as the weight (*Materials and Methods*). Fig. 1A shows a decreasing trend in both satellite-inferred and modeled multimonth mean Arctic surface albedo from 1982 to 2014. The trend from 2 AVHRR-inferred surface albedos is -1.25 ± 0.34 and $-1.51 \pm 0.41\%$ decade⁻¹, respectively, somewhat steeper than that derived from the CAM5 simulation ($-0.89 \pm 0.26\%$ decade⁻¹). The CAM5 surface albedo is mostly in between the 2 AVHRR-inferred surface albedos with a correlation coefficient (R) larger than 0.8. All of the trends and the correlation coefficients are statistically significant at the 99% confidence level. Relative mean bias (RMB) of modeled surface albedo with respect to the 2 AVHRR surface albedo estimates is -1% and 2% , respectively. There is a large spread between the 2 satellite products, indicating remaining uncertainties in the satellite-inferred surface albedo trends. Fewer assumptions are needed in retrievals of top of atmosphere (TOA) planetary albedo than in the satellite-inferred surface albedo. Here we also include a comparison of CAM5 results to CERES-based TOA albedo product over Arctic oceanic areas poleward of 60°N (40). The CAM5-simulated planetary albedo trend of $-0.84 \pm 0.19\%$ decade⁻¹ for 1980 to 2014 agrees well with the CERES-based estimate ($-0.88 \pm 0.17\%$ decade⁻¹) in Fig. 1B (trends and the correlation coefficient are statistically significant at the 99% confidence level). The RMB of CAM5 planetary albedo is -2% . Taking into account the uncertainties in the satellite-derived products, the CAM5 model with prescribed sea ice gives a reasonable estimate of the Arctic albedo and trend.

The satellite-model comparison is based on March through September mean results. Before we use the CAM5 simulation to perform the attribution analysis, the annual-mean surface albedo over the Arctic during 1980 to 2014 is further evaluated against reanalysis products (*SI Appendix, Fig. S1*). The trend

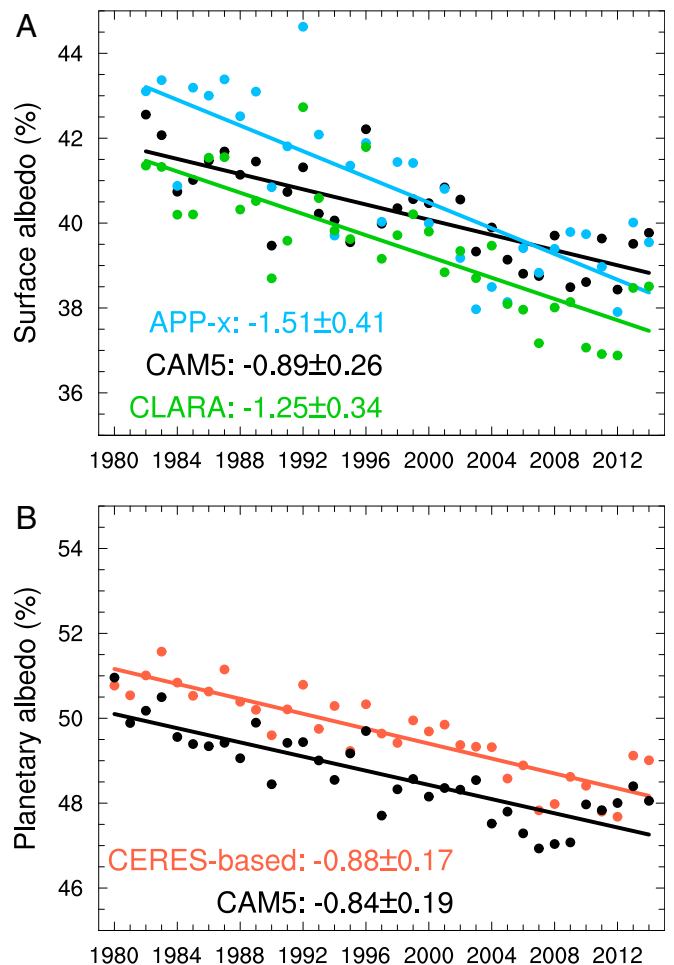


Fig. 1. Albedo trend. Area- and energy-weighted average of multimonth (March to September of each year) mean (A) surface albedo over the entire Arctic and (B) planetary albedo over the Arctic oceanic area (north of 60°N). The solid lines are linear least-squares fit to the corresponding time series with the trend (in % decade⁻¹) marked in colors with the 95% confidence interval as uncertainty at the bottom. All trends are statistically significant at the 99% confidence level. In A the black, blue, and green dots are, respectively, CAM5 model results, APP-x, and CLARA-A2 satellite-inferred surface albedo from 1982 to 2014. The correlation coefficient (R) between CAM5 and APP-x results is 0.8 ($P < 0.01$) and the RMB of the simulation is -1% . The R between CAM5 and CLARA-A2 results is 0.88 ($P < 0.01$) and the RMB of the simulation is 2% . In B the red and black dots are CERES and CAM5 planetary albedo from 1980 to 2014, respectively. The R between CAM5 and CERES results is 0.85 ($P < 0.01$) and the RMB of the simulation is -2% .

of -0.96% decade⁻¹ in the CAM5 simulation is within the range of $(-0.7, -1)\%$ decade⁻¹ given by 3 different reanalysis products. Thus, the model simulation, satellite datasets, and reanalysis products all indicate an $\sim 1\%$ decade⁻¹ decreasing trend in annual-mean surface albedo over the Arctic since the 1980s, but the primary contributor to this albedo reduction is not obvious.

Surface Albedo Trend Attribution. Given the important role of both snow cover and sea ice in surface albedo, detailed and internally consistent CAM5 results can be used to attribute the contributions from snow cover fraction (SCF) and sea ice fraction over the Arctic (Fig. 2). The surface of each model grid may include bare land, snow, sea ice, and/or open ocean, for which the albedo varies and cannot be directly isolated from the grid mean radiative fluxes. To perform the attribution

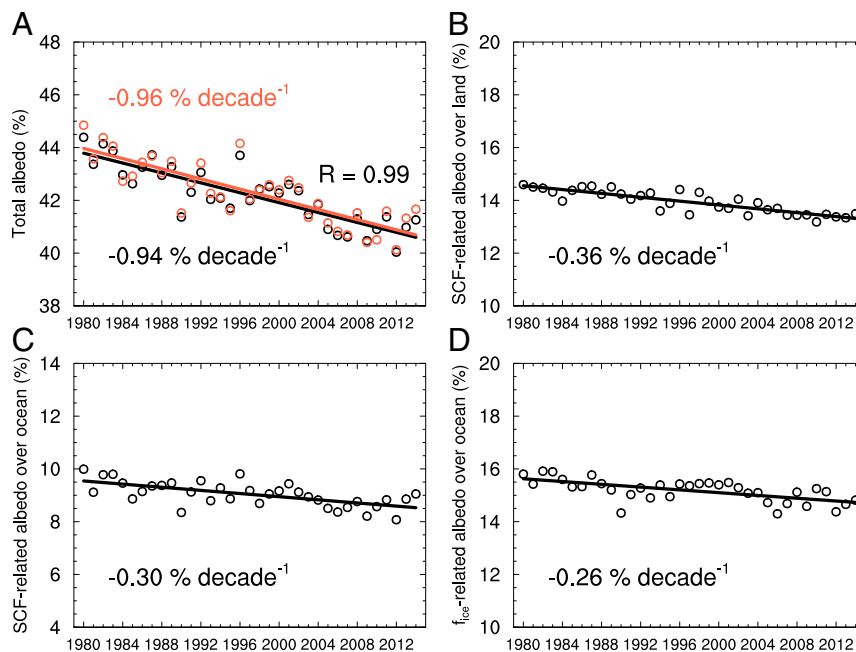


Fig. 2. Surface albedo trend and attribution. (A) Time evolution of area- and energy-weighted average of annual-mean surface albedo over the Arctic during 1980 to 2014 from CAM5 (red) as well as using a surrogate model (black). The Arctic albedos derived from these 2 methods are highly correlated ($R = 0.99$, $P < 0.01$). (B) Contributions to surface albedo trend from SCF change over Arctic land. (C) Same as B but over Arctic ocean. (D) Same as C but for contributions from sea ice fraction change. In all panels, the solid line is a linear least-squares fit, of which the slope represents the trend in units of $\% \text{ decade}^{-1}$ (marked in each panel). All of the regression coefficients are statistically significant at the 99% confidence level.

analysis of trends in total albedo we express the monthly grid mean albedo (α) in the form

$$\alpha = SCF \cdot f_{land} \cdot \alpha_{land}^{snow} + (1 - SCF) \cdot f_{land} \cdot \alpha_{land} + (1 - f_{land} - f_{ice}) \cdot \alpha_{ocean} + SCF \cdot f_{ice} \cdot \alpha_{ice}^{snow} + (1 - SCF) \cdot f_{ice} \cdot \alpha_{ice}, \quad [1]$$

where SCF , f_{land} , and f_{ice} are monthly mean snow cover fraction, land fraction, sea ice fraction for a given grid cell, respectively; and α_{land}^{snow} , α_{land} , α_{ocean} , α_{ice}^{snow} , and α_{ice} denote albedo of snow-covered land, snow-free land, open ocean, snow-covered sea ice, and snow-free sea ice, respectively. Mean values for α_{ocean} , α_{ice}^{snow} , and α_{ice} are determined to be 7.88%, 84.08%, and 30.91%. Annual-mean climatology of α_{land} and monthly mean climatology of α_{land}^{snow} are quantified at each grid cell where $f_{land} > 0$ (*Materials and Methods* and *SI Appendix, Fig. S2*). The physically based surrogate model in Eq. 1 can reproduce the annual-mean surface albedo over the Arctic from CAM5 (Fig. 2A). Thus, the decreasing trend in annual-mean surface albedo can be attributed to reductions in snow cover fraction and sea ice fraction (*Materials and Methods*). The surrogate model gives a surface albedo trend of $-0.94\% \text{ decade}^{-1}$ (Fig. 2A), among which 70% (i.e., $-0.66\% \text{ decade}^{-1}$) is attributed to snow cover fraction change, with 38% over land ($-0.36\% \text{ decade}^{-1}$ in Fig. 2B) and 32% over sea ice ($-0.3\% \text{ decade}^{-1}$ in Fig. 2C), while the sea ice fraction retreat explains the remaining 30% ($-0.26\% \text{ decade}^{-1}$ in Fig. 2D). Our results appear inconsistent with a recent observational study (19) that suggests a more important impact of sea ice than snow cover on Arctic albedo reduction. This is because that study attributes all changes over ocean to the sea ice. Here we identify a nearly equally important role of snow cover fraction changes over sea ice compared to sea ice cover changes themselves and compared to terrestrial snow cover changes. Given the importance of surface air temperature (SAT) and snowfall to snow cover fraction, we turn

next to an assessment of trends in SAT and precipitation/snowfall over the Arctic.

Attribution of Snow Cover Fraction Changes. *SI Appendix, Figs. S3 and S4* illustrate the trends of anomalous area-averaged annual-mean Arctic SAT and total precipitation relative to the 1980 to 2014 mean. The CAM5 precipitation rate shows an increasing trend ($6.93 \text{ mm decade}^{-1}$) as the Arctic warms ($0.43 \text{ K decade}^{-1}$ for SAT). However, the area-averaged annual-mean snowfall exhibits a decreasing trend from 1980 to 2014 (*SI Appendix, Fig. S5A*). The results of 3 different reanalysis products show similar increasing trends in SAT and total precipitation (*SI Appendix, Figs. S3 and S4*) as well as decreasing trends in snowfall (*SI Appendix, Fig. S5*). The CAM5 trends are all well within the ranges defined by the reanalysis results. The trend of $6.93 \text{ mm decade}^{-1}$ in the Arctic total precipitation from CAM5 (*SI Appendix, Fig. S4A*) also agrees well with the trend of $7.13 \text{ mm decade}^{-1}$ from the GPCP (Global Precipitation Climatology Project) observations (*SI Appendix, Fig. S4E*).

We have identified the reduction in snow cover fraction as the primary contributor to the decreasing trend in annual-mean surface albedo (Fig. 2). Here, we further show what determines the reduction in snow cover fraction. A recent study (41) has suggested that the midlatitude land SAT can explain $\sim 50\%$ of the variance in Northern Hemisphere land snow cover during the spring of 1922 to 2010. Physically the variation in snow cover is closely related to changes in air temperature and snowfall at the surface. The former affects snow melting while the latter is the main source of snow cover. However, there is no simple physically based equation to directly relate the 3 quantities, so we derive their relationship based on a statistical analysis. To maintain the consistency with Fig. 2, the snow cover area (SCA) fraction is defined as the ratio of SCA to the entire Arctic surface area with a fixed sea ice fraction. Thus, the SCA is calculated as the following summation over grid cells within the Arctic: $SCA = \sum SCF \cdot (f_{land} + f_{ice}) \cdot A$, where A

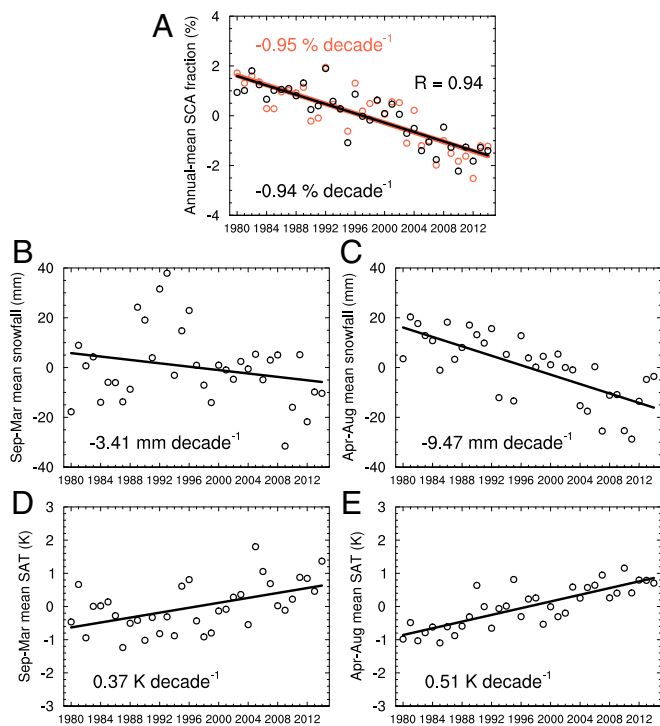


Fig. 3. Trend and attribution of snow cover area fraction. (A) Anomalies of annual-mean Arctic SCA fraction relative to 1980 to 2014 climatology with fixed sea ice fraction from CAM5 (red) and multiregression method (black). The 2 SCA fractions are highly correlated ($R = 0.94$, $P < 0.01$). (B) Anomalies of area-weighted average of Arctic mean snowfall during the accumulation season (September to March). (C) Same as B, but for the melting season (April to August). (D) Anomalies of area-weighted average of Arctic mean SAT during the accumulation season. (E) Same as D, but for the melting season. In all panels, the solid line represents a linear least-squares fit. The linear trend with units is marked for each panel. Except for the regression coefficient in panel B where P value is 0.17, all of the regression coefficients are statistically significant at the 99% confidence level.

represents grid cell area and $\overline{f_{ice}}$ is monthly mean climatology of f_{ice} . The anomalies of annual-mean SCA fraction are shown in Fig. 3A (red circles) with a trend of $-0.95\% \text{ decade}^{-1}$ (red line). Given the strong and distinct seasonal cycle of SCA fraction (SI Appendix, Fig. S6), we define September to March as the snow-accumulation season and April to August as the snow-melting season. To attribute the trend of annual-mean SCA fraction, a multiple linear regression analysis is performed using the anomaly of annual-mean SCA fraction (denoted as F) as the dependent variable and anomalies of seasonal-mean snowfall and SAT as independents. The regression equation is obtained as $F = 0.019 \cdot S_a + 0.024 \cdot S_m - 0.258 \cdot T_a - 1.089 \cdot T_m - 5 \cdot 10^{-6}$, where S_a, S_m, T_a , and T_m are the anomalies of accumulation-season mean and melting-season mean of snowfall and SAT over the Arctic, respectively. The anomalies of S_a, S_m, T_a , and T_m and their trends are shown in Fig. 3 B, C, D, and E, respectively. Based on the regression equation, we obtain the dependent F and its trend ($-0.94\% \text{ decade}^{-1}$), as shown in Fig. 3A (black circles and line). F has a strong correlation ($R = 0.94$) with the model-simulated SCA fraction, and their trends are almost identical, suggesting that the variation in SCA fraction can be fully explained by SAT and snowfall. Furthermore, the contributions of 7, 24, 10, and 59% to the trend in F by S_a, S_m, T_a , and T_m , respectively, are quantified based on the corresponding regression coefficients and their trends. Therefore, the decreasing trend of SCA fraction is largely determined by the increase of SAT (69%) and decrease in snowfall (31%) over the Arctic, especially during the snow-melting season.

Role of Absorbing Soot Deposition. Impurities such as soot in snow can significantly reduce snow albedo due to the high albedo of pristine snow at visible wavelengths (27). Some modeling studies have suggested that one of the reasons for the Arctic warming is that soot strongly absorbs solar radiation in the atmosphere and snowpack (42). However, atmospheric soot concentrations and deposition fluxes have been declining in the Arctic since the 1980s, as shown at remote surface stations (43–45) and in ice core data (46). Based on the CAM5 simulation, we are able to calculate the trend in deposition flux and soot-in-snow concentration/forcing. Note that soot-in-snow results are based on the SNICAR (SNOW, Ice, and Aerosol Radiative) model (47), which is coupled to CAM5 and embedded in the land component of the Community Earth System Model. Compared to the observed soot concentration in surface snow (30), the modeled soot RMB is about 27.6% (SI Appendix, Fig. S7B). This indicates that the model likely overestimates the effect of soot in the Arctic snow/ice. The evaluation of the trend in concentration in surface air is described in SI Appendix, Supplementary Text. There was a decreasing trend in area-averaged annual-mean concentration over Arctic land in the CAM5 simulation over the period 1980 to 2014 (SI Appendix, Fig. S7C).

How does the change in soot-in-snow forcing compare to the change in radiative flux due to surface albedo reduction? As expected from the decreased snow cover and surface albedo, the area-averaged annual-mean solar flux absorbed over the Arctic land surface increased from 1980 to 2014 (SI Appendix, Fig. S9B). In contrast, the snow forcing over Arctic land from soot decreased during this period (SI Appendix, Fig. S9A). In addition, the ratio of the soot-in-snow forcing to net absorbed solar flux at surface is less than 1% (SI Appendix, Fig. S9C). The total decrease in the positive forcing from 1980 to 2014, estimated using the trend multiplied by the time interval, is 0.17 W m^{-2} , which is overwhelmed by the overall increase of 3.5 W m^{-2} in net surface shortwave flux over Arctic land. While the spatial distribution of annual-mean soot deposition trends (Fig. 4A) shows a weak increase in northern Canada, Alaska, and northeastern Russia, strong and significant decreasing trends appear in the regions from the east of Greenland through northern Europe to Siberia, especially over the land regions. Overall, the trend of area-averaged annual-mean soot deposition over the Arctic (Fig. 4B) is negative, with an abrupt decline during 1991 to 1993, which is related to the dissolution of the former Soviet Union (45). Our analysis thus does not support the argument that deposition of soot on snow caused the decline of Arctic snow and ice cover, and consequently the Arctic amplification since the 1980s.

Summary

Results from a global aerosol-climate model (CAM5) along with satellite data, reanalysis data, and field data are used to explore the trends in surface albedo, snow cover fraction, temperature, snowfall, and soot deposition during 1980 to 2014 in the Arctic (60 to 90°N). Our results suggest that the increase in surface air temperature along with the decrease in snowfall is mainly responsible for the decrease in annual-mean snow cover fraction over the Arctic land and sea ice, explaining $\sim 70\%$ of the reduction in Arctic annual-mean surface albedo while the reduced sea ice fraction is responsible for most of the remaining. The declining trends in soot deposition, its concentration in snow, and the associated forcing during 1980 to 2014 suggest that this process has not been the driver for the decrease in Arctic surface albedo and the increase in Arctic warming since the 1980s.

Materials and Methods

Model and Data. The global aerosol-climate model used in this study is a variant of the CAM5 (48), that is also the atmospheric component of the Community Earth System Model (CESM) (49). The model includes revisions to the treatment of aerosol-cloud processes to better characterize the vertical

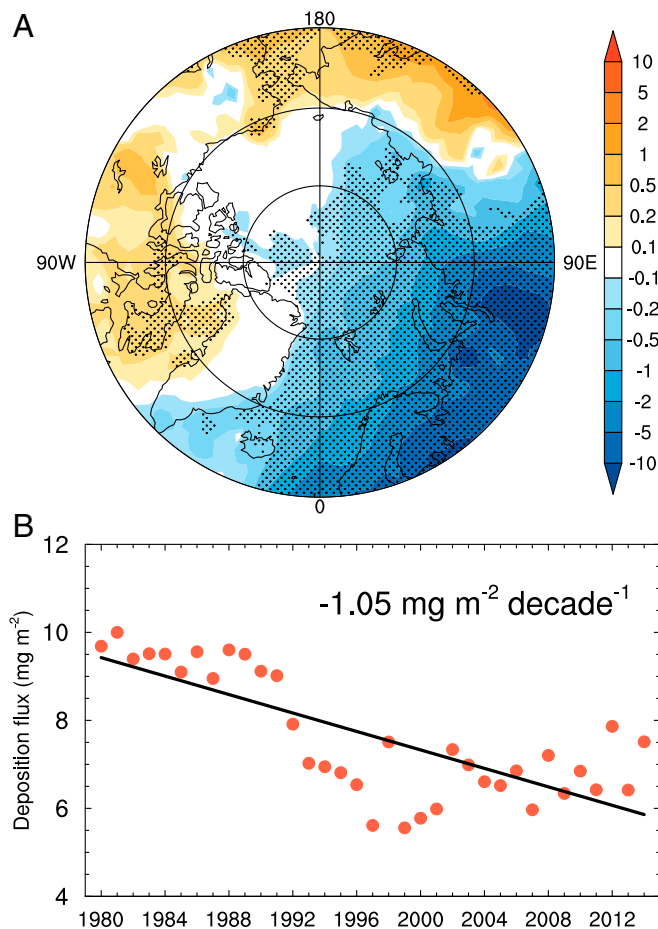


Fig. 4. Soot deposition trend. (A) Spatial distribution of linear trends ($\text{mg m}^{-2} \text{decade}^{-1}$) in annual-mean soot deposition during 1980 to 2014. Stippling indicates statistical significance at the 95% confidence level using Student's t test. (B) Area-averaged annual-mean soot deposition (mg m^{-2}) over the Arctic from 1980 to 2014. The black line is a linear least-square regression and the trend is statistically significant at the 99% confidence level.

redistribution and removal of aerosols as they are transported to remote regions, such as the Arctic (50), and a 4-mode version of the Modal Aerosol Module (51) with an additional primary-carbon mode that also improves the simulation of near-surface absorbing aerosol-mixing ratio in the Arctic (51).

A 36-y CAM5 simulation (1979 to 2014) was conducted at a horizontal grid spacing of 1.9° (latitude) by 2.5° (longitude) and with 30 vertical levels up to 3.6 hPa. Observed monthly mean sea-surface temperatures and sea ice concentrations were prescribed to the model, while the land component including snow and ice over the land surface is interactive. To minimize the impact of model bias in simulating large-scale circulations, wind fields are constrained with reanalysis from NASA Modern Era Retrospective-Analysis for Research and Applications (MERRA) (52, 53). Monthly mean anthropogenic and open biomass burning emissions from the recently released datasets (36, 38) for the Coupled Model Intercomparison Project Phase 6 are used in the simulation following ref. 54. Model results of 35 y during 1980 to 2014 were analyzed in this study with the first model year considered as the spin-up and excluded.

In addition to the CAM5 simulation, we use the Japanese 55-y reanalysis (JRA-55) provided by the Japan Meteorological Agency (55), the ERA-Interim reanalysis provided by ECMWF (European Centre for Medium-Range Weather Forecasts) (56), and the MERRA-2 (version 2) reanalysis provided by NASA (57). We also use the latest GPCP (version 2.3) monthly precipitation data set (1979 to 2014) combined with ground and satellite precipitation data (58, 59). Two monthly surface albedo datasets derived from the AVHRR sensor were used: 1) the Extended AVHRR Polar Pathfinder (APP-x) satellite products (60) and 2) the 2nd edition of the satellite-derived climate data record CLARA-A2 (61). Both surface albedo datasets cover the same period from 1982 to 2014. Planetary (top of atmosphere) albedo over the Arctic

oceanic area is based on CERES Terra Single Scanner Footprint Ed4A monthly averaged 1° product during the CERES period (2000 to 2016) following ref. 40. Following that study, for the pre-CERES period (1979 to 1999), the planetary albedo was reconstructed using the observed ice concentration (1979 to 1999) based on a linear approximation of the relationship between planetary albedo and ice cover during 2000 to 2016.

Calculation of Annual-Mean Arctic Surface Albedo. For each grid cell, the annual-mean surface albedo is calculated as

$$\bar{\alpha} = \frac{\sum \alpha \cdot D}{\sum D}, \quad [2]$$

where α is surface albedo at each grid for each month. D is the downwelling shortwave flux at the surface. The summation is over all months of the year when $D > 0$.

An annual averaged-area weighted albedo is also estimated for the whole Arctic from the gridded monthly values,

$$\bar{\alpha} = \frac{\sum \sum \alpha \cdot D \cdot A}{\sum \sum D \cdot A}, \quad [3]$$

where A is the cell area. The inner summation is again over all months of the year where $D > 0$. The outer summation is over all cells within the Arctic (60 to 90°N) when $D > 0$.

Attribution of Annual-Mean Arctic Surface Albedo Changes. The total surface albedo within each cell in the Arctic for each month during 1980 to 2014 is estimated as

$$\alpha_0 = U/D, \quad [4]$$

where U and D denote the upwelling and downwelling shortwave flux at the surface, respectively, from the CAM5 output.

The surface of each model grid cell may include bare land, snow, sea ice, and/or open ocean, for which the albedo varies and cannot be directly isolated using the grid mean radiative fluxes. To perform the attribution analysis of trends in surface albedo, we first build a physics-based surrogate model to estimate grid mean albedo α from various components, as shown in Eq. 1.

Based on the α_0 at each grid for each month, we then quantify the mean albedo of each component (surface type) for Eq. 1 as follows:

- 1) For α_{ocean} , we first sample the cells where $f_{\text{ice}} = 0$ and $f_{\text{land}} = 0$, and then derive α_{ocean} from the formula $\alpha_0 = \alpha_{\text{ocean}}$. The probability distribution functions (PDF) analysis is plotted in *SI Appendix, Fig. S2A*. The mean of α_{ocean} is 7.88%.
- 2) For $\alpha_{\text{ice}}^{\text{snow}}$, we first sample the grids where $f_{\text{ice}} = 1$ and $\text{SCF} = 1$, and then derive $\alpha_{\text{ice}}^{\text{snow}}$ from the formula $\alpha_0 = \alpha_{\text{ice}}^{\text{snow}}$. The PDF analysis is plotted in *SI Appendix, Fig. S2B*. The mean of $\alpha_{\text{ice}}^{\text{snow}}$ is 84.08%.
- 3) For α_{ice} , we first sample the grids where $f_{\text{land}} = 0$, and then derive α_{ice} from the formula $\alpha_0 = \text{SCF} \cdot f_{\text{ice}} \cdot \alpha_{\text{ice}}^{\text{snow}} + (1 - \text{SCF}) \cdot f_{\text{ice}} \cdot \alpha_{\text{ice}} + (1 - f_{\text{ice}}) \cdot \alpha_{\text{ocean}}$ based on $\alpha_{\text{ocean}} = 7.88\%$ and $\alpha_{\text{ice}}^{\text{snow}} = 84.08\%$. In the CESM model, the snow-free sea ice includes bare ice and melt ponds (62). The bare ice albedo values are $\sim 60\%$, but melt ponds albedos range from 10 to 70% (25). Thus, the grids where $\alpha_{\text{ice}} < 10\%$ and $\alpha_{\text{ice}} > 70\%$ are excluded in the calculation. The PDF analysis is plotted in *SI Appendix, Fig. S2C*. The mean of α_{ice} is 30.91%.
- 4) For α_{land} , we first sample the grids where $f_{\text{ice}} = 0$ and $\text{SCF} = 0$, and then derive α_{land} from the formula $\alpha_0 = f_{\text{land}} \cdot \alpha_{\text{land}} + (1 - f_{\text{land}}) \cdot \alpha_{\text{ocean}}$ based on $\alpha_{\text{ocean}} = 7.88\%$. Here α_{land} at some grids cannot be obtained due to the presence of perpetual snow cover even in the summer. We also found that the α_{land} is biased high over some grids where f_{land} is very small and there is perpetual land ice cover. A previous study (63) shows that the maximum annual-mean snow-free land surface albedo is 26% over the ice cover area (e.g., the edge of Greenland) within the Arctic from satellite datasets. Thus, the grids where $\alpha_{\text{land}} < 0$ and $\alpha_{\text{land}} > 26\%$ are excluded in the calculation. Finally, we calculate the average of α_{land} at each grid and then set $\alpha_{\text{land}} = 26\%$ wherever there is a missing value but $f_{\text{land}} > 0$. In this way, we have individual values for α_{land} at each grid where $f_{\text{land}} > 0$ (*SI Appendix, Fig. S2D*).
- 5) Based on the above analysis, we derived α_{ocean} , $\alpha_{\text{ice}}^{\text{snow}}$, α_{ice} , and α_{land} at each grid. The $\alpha_{\text{land}}^{\text{snow}}$ is calculated by using Eqs. 4 and 1 when $\text{SCF} \cdot f_{\text{land}} > 0.01$ to avoid the biased high values for $\alpha_{\text{land}}^{\text{snow}}$ in the summer months. The upper limit of snow albedo is 90% for fresh snow (25). Thus, we exclude the grids where $\alpha_{\text{land}}^{\text{snow}} < \alpha_{\text{land}}$ and $\alpha_{\text{land}}^{\text{snow}} > 90\%$. Finally, we calculate the monthly mean climatology of $\alpha_{\text{land}}^{\text{snow}}$ at each grid and then set $\alpha_{\text{land}}^{\text{snow}} = \alpha_{\text{land}}$ wherever there is a missing value but $f_{\text{land}} > 0$. Based on

the monthly climatology of α_{land}^{snow} . *SI Appendix, Fig. S2E* shows the spatial distribution of its annual mean calculated by Eq. 2 using CAM5 monthly mean climatology of surface downwelling shortwave flux as the energy weight.

In this way we derive α_{ocean} , α_{ice}^{snow} , α_{ice} , α_{land} , and monthly mean climatology of α_{land}^{snow} at each grid within the Arctic for Eq. 1. To further check the difference of albedo derived from Eqs. 4 and 1, we plot the PDF of their difference (i.e., $\alpha_0 - \alpha$) in *SI Appendix, Fig. S2F*, which shows a mean value close to zero.

Using the derived mean albedos for different surface types, we first calculate the total surface albedo within each grid in the Arctic for each month during 1980 to 2014 based on Eq. 1. Then the annual-mean surface albedo over the Arctic is calculated by Eq. 3. Finally, the trend of annual-mean albedo over the Arctic can be decomposed into the following terms:

$$\frac{\Delta[\alpha]}{\Delta t} = \frac{\Delta \left[SCF \cdot \overline{f_{land}} \cdot (\alpha_{land}^{snow} - \alpha_{land}) + SCF \cdot \overline{f_{ice}} \cdot (\alpha_{ice}^{snow} - \alpha_{ice}) \right]}{\Delta t} + \frac{\Delta \left[SCF \cdot \overline{f_{ice}} \cdot (\alpha_{ice}^{snow} - \alpha_{ice}) + f_{ice} \cdot (\alpha_{ice} - \alpha_{ocean}) \right]}{\Delta t} \quad [5]$$

where square brackets are used to enclose quantities for area- and energy-weighted average of annual-mean values by Eq. 3. The overbar on *SCF* or f_{ice} represents its monthly mean climatology of 1980 to 2014 at each grid. The trend (operator $\Delta/\Delta t$) can be estimated as the slope of a linear least-squares fit to 35 annual mean values of the variable. The first and second terms on the right-hand side of Eq. 5 represent contributions to the trend of albedo by *SCF* changes and f_{ice} changes, respectively.

1. M. C. Serreze, R. G. Barry, Processes and impacts of Arctic amplification: A research synthesis. *Global Planet. Change* **77**, 85–96 (2011).
2. J. Cohen *et al.*, Recent Arctic amplification and extreme mid-latitude weather. *Nat. Geosci.* **7**, 627–637 (2014).
3. Intergovernmental Panel on Climate Change (IPCC), *Climate Change 2013: The Physical Science Basis, in Contribution of Working Group I to the Fifth Assessment Report of the Intergovernmental Panel on Climate Change*, T. F. Stocker *et al.*, Eds. (Cambridge University Press, Cambridge, UK, 2013).
4. M. M. Holland, C. M. Bitz, Polar amplification of climate change in coupled models. *Clim. Dyn.* **21**, 221–232 (2003).
5. R. G. Graversen, M. Wang, Polar amplification in a coupled climate model with locked albedo. *Clim. Dyn.* **33**, 629–643 (2009).
6. J. Brigham-Grette *et al.*, Pliocene warmth, polar amplification, and stepped Pleistocene cooling recorded in NE Arctic Russia. *Science* **340**, 1421–1427 (2013).
7. A. M. Haywood *et al.*, Large-scale features of Pliocene climate: Results from the Pliocene Model Intercomparison Project. *Clim. Past* **9**, 191–209 (2013).
8. F. Pithan, T. Mauritsen, Arctic amplification dominated by temperature feedbacks in contemporary climate models. *Nat. Geosci.* **7**, 181–184 (2014).
9. S. Manabe, R. J. Stouffer, Sensitivity of a global climate model to an increase of CO₂ concentration in the atmosphere. *J. Geophys. Res.* **85**, 5529–5554 (1980).
10. J. A. Curry, J. L. Schramm, E. E. Ebert, Sea ice-albedo climate feedback mechanism. *J. Clim.* **8**, 240–247 (1995).
11. M. Winton, Amplified Arctic climate change: What does surface albedo feedback have to do with it? *Geophys. Res. Lett.* **33**, L03701 (2006).
12. J. A. Screen, I. Simmonds, The central role of diminishing sea ice in recent Arctic temperature amplification. *Nature* **464**, 1334–1337 (2010).
13. S. R. Hudson, Estimating the global radiative impact of the sea ice-albedo feedback in the Arctic. *J. Geophys. Res.* **116**, D16102 (2011).
14. P. C. Taylor *et al.*, A decomposition of feedback contributions to polar warming amplification. *J. Clim.* **26**, 7023–7043 (2013).
15. R. Zhang *et al.*, Local radiative feedbacks over the Arctic based on observed short-term climate variations. *Geophys. Res. Lett.* **45**, 5761–5770 (2018).
16. S. Bony *et al.*, How well do we understand and evaluate climate change feedback processes? *J. Clim.* **19**, 3445–3481 (2006).
17. X. Wang, J. R. Key, Recent trends in Arctic surface, cloud, and radiation properties from space. *Science* **299**, 1725–1728 (2003).
18. X. Chen, S. Liang, Y. Cao, T. He, D. Wang, Observed contrast changes in snow cover phenology in northern middle and high latitudes from 2001–2014. *Sci. Rep.* **5**, 16820 (2015).
19. A. Letterly, J. Key, Y. Liu, Arctic climate: Changes in sea ice extent outweigh changes in snow cover. *Cryosphere* **12**, 3373–3382 (2018).
20. I. M. Held, B. J. Soden, Robust responses of the hydrological cycle to global warming. *J. Clim.* **19**, 5686–5699 (2006).
21. P. C. Taylor *et al.*, “Arctic changes and their effects on Alaska and the rest of the United States” in *Climate Science Special Report: Fourth National Climate Assessment*, D. J. Wuebbles *et al.*, Eds. (US Global Climate Change Research Program, Washington, DC, 2017), vol. 1, pp. 303–332.
22. D. J. Wuebbles *et al.*, “Our globally changing climate” in *Climate Science Special Report: Fourth National Climate Assessment*, D. J. Wuebbles *et al.*, Eds. (US Global Climate Change Research Program, Washington, DC, 2017), vol. 1, pp. 35–72.

Data and Materials Availability. The MERRA reanalysis can be found at <https://disc.gsfc.nasa.gov/mdisc/>. The JRA-55 reanalysis is obtained from https://jra.kishou.go.jp/JRA-55/index_en.html. The ERA-Interim reanalysis is acquired from <https://apps.ecmwf.int/datasets/data/interim-full-mode/levtype=pl/>. GPCP Precipitation data are provided by the Physical Sciences Division of Earth System Research Laboratory, Oceanic and Atmospheric Research, National Oceanic and Atmospheric Administration, Boulder, CO, from their website at <https://www.esrl.noaa.gov/psd/>. The AVHRR APP-x satellite data can be found at <https://data.nodc.noaa.gov/cgi-bin/iso?id=gov.noaa.ncdc:C00941>. The satellite-based surface albedo data (CLARA-A2) can be found at https://wui.cmsaf.eu/safira/action/viewDoiDetails?acronym=CLARA_AVHRR_V002. CAM5 model data are available at https://release.datahub.pnnl.gov/released_data/990.

ACKNOWLEDGMENTS. We thank Stephen Warren and Sarah Doherty for very helpful comments on an earlier version of the paper; Kristina Pistone for providing the CERES TOA albedo data; Po-Lun Ma for providing MERRA reanalysis data used in the CAM5 simulation; and Vincent Dutkiewicz for providing the airborne soot measurement data at the Kevo site. We also thank Richard Bintanja, Elizabeth Hunke, and David Bailey for helpful communications. This work was based on research supported by the US Department of Energy (DOE), Office of Science, Biological and Environmental Research, as part of the Regional and Global Model Analysis program. The Pacific Northwest National Laboratory (PNNL) is operated for DOE by Battelle Memorial Institute under Contract DE-AC05-76RLO1830. The model simulations were performed using PNNL Institutional Computing resources.

23. R. Bintanja, F. M. Selten, Future increases in Arctic precipitation linked to local evaporation and sea-ice retreat. *Nature* **509**, 479–482 (2014).
24. R. Bintanja, O. Andry, Towards a rain-dominated Arctic. *Nat. Clim. Chang.* **7**, 263–267 (2017).
25. D. K. Perovich, T. C. Grenfell, B. Light, P. V. Hobbs, Seasonal evolution of the albedo of multiyear Arctic sea ice. *J. Geophys. Res.* **107**, 8044 (2002).
26. S. G. Warren, Optical-properties of snow. *Rev. Geophys.* **20**, 67–89 (1982).
27. S. G. Warren, W. J. Wiscombe, A model for the spectral albedo of snow. II: Snow containing atmospheric aerosols. *J. Atmos. Sci.* **37**, 2734–2745 (1980).
28. T. C. Bond *et al.*, Bounding the role of black carbon in the climate system: A scientific assessment. *J. Geophys. Res. Atmos.* **118**, 5380–5552 (2013).
29. A. D. Clarke, K. J. Noone, Soot in the Arctic snowpack: A cause for perturbations in radiative transfer. *Atmos. Environ.* **19**, 2045–2053 (1985).
30. S. J. Doherty, S. G. Warren, T. C. Grenfell, A. D. Clarke, R. E. Brandt, Light-absorbing impurities in Arctic snow. *Atmos. Chem. Phys.* **10**, 11,647–11,680 (2010).
31. R. E. Brandt, S. G. Warren, A. D. Clarke, A controlled snowmaking experiment testing the relation between black carbon content and reduction of snow albedo. *J. Geophys. Res.* **116**, D08109 (2011).
32. R. Zhang, D. A. Hegg, J. Huang, Q. Fu, Source attribution of insoluble light-absorbing particles in seasonal snow across northern China. *Atmos. Chem. Phys.* **13**, 6091–6099 (2013).
33. S. J. Doherty, C. Dang, D. A. Hegg, R. Zhang, S. G. Warren, Black carbon and other light-absorbing particles in snow of central North America. *J. Geophys. Res. Atmos.* **119**, 12,807–12,831 (2014).
34. C. Dang *et al.*, Measurements of light-absorbing particles in snow across the Arctic, North America, and China: Effects on surface albedo. *J. Geophys. Res. Atmos.* **122**, 10,149–10,168 (2017).
35. M. Jeffries, J. E. Overland, D. K. Perovich, The Arctic shifts to a new normal. *Phys. Today* **66**, 35–40 (2013).
36. R. M. Hoesly *et al.*, Historical (1750–2014) anthropogenic emissions of reactive gases and aerosols from the Community Emission Data System (CEDS). *Geosci. Model Dev.* **11**, 369–408 (2018).
37. H. Wang *et al.*, Using an explicit emission tagging method in global modeling of source-receptor relationships for black carbon in the Arctic: Variations, sources, and transport pathways. *J. Geophys. Res. Atmos.* **119**, 12,888–12,909 (2014).
38. M. J. E. van Marle *et al.*, Historic global biomass burning emissions for CMIP6 (BB4CMIP) based on merging satellite observations with proxies and fire models (1750–2015). *Geosci. Model Dev.* **10**, 3329–3357 (2017).
39. K. Pistone, I. Eisenman, V. Ramanathan, Observational determination of albedo decrease caused by vanishing Arctic sea ice. *Proc. Natl. Acad. Sci. U.S.A.* **111**, 3322–3326 (2014).
40. K. Pistone, I. Eisenman, V. Ramanathan, Radiative heating of an ice-free arctic ocean. *Geophys. Res. Lett.* **46**, 7474–7480 (2019).
41. R. Brown, D. Robinson, Northern Hemisphere spring snow cover variability and change over 1922–2010 including an assessment of uncertainty. *Cryosphere* **5**, 219–229 (2011).
42. AMAP, *AMAP Assessment 2015: Black carbon and ozone as Arctic climate forcers* (Arctic Monitoring and Assessment Programme, Oslo, Norway, 2015).
43. S. L. Gong *et al.*, Identification of trends and interannual variability of sulphate and black carbon in the Canadian High Arctic: 1981 to 2007. *J. Geophys. Res.* **115**, D07305 (2010).

44. D. Hirdman *et al.*, Long-term trends of black carbon and sulphate aerosol in the Arctic: Changes in atmospheric transport and source region emissions. *Atmos. Chem. Phys.* **10**, 9351–9368 (2010).
45. S. Sharma *et al.*, 16-year simulation of Arctic black carbon: Transport, source contribution, and sensitivity analysis on deposition. *J. Geophys. Res. Atmos.* **118**, 943–964 (2013).
46. S. E. Bauer *et al.*, Historical and future black carbon deposition on the three ice caps: Ice core measurements and model simulations from 1850 to 2100. *J. Geophys. Res. Atmos.* **118**, 7948–7961 (2013).
47. M. G. Flanner, C. S. Zender, J. T. Randerson, P. J. Rasch, Present-day climate forcing and response from black carbon in snow. *J. Geophys. Res.* **112**, D11202 (2007).
48. R. B. Neale *et al.*, "Description of the NCAR Community Atmosphere Model (CAM5)" Tech. Rep. NCAR/TN-486+STR (National Center for Atmospheric Research, Boulder, CO, 2010).
49. J. W. Hurrell *et al.*, The community earth system model: A framework for collaborative research. *Bull. Am. Meteorol. Soc.* **94**, 1339–1360 (2013).
50. H. Wang *et al.*, Sensitivity of remote aerosol distributions to representation of cloud-aerosol interactions in a global climate model. *Geosci. Model Dev.* **6**, 765–782 (2013).
51. X. Liu *et al.*, Description and evaluation of a new 4-mode version of Modal Aerosol Module (MAM4) within version 5.3 of the Community Atmosphere Model. *Geosci. Model Dev.* **9**, 505–522 (2016).
52. M. M. Rienecker *et al.*, MERRA: NASA's modern-era retrospective analysis for research and applications. *J. Clim.* **24**, 3624–3648 (2011).
53. P.-L. Ma *et al.*, The role of circulation features on black carbon transport into the Arctic in the Community Atmosphere Model version 5 (CAM5). *J. Geophys. Res. Atmos.* **118**, 4657–4669 (2013).
54. Y. Yang *et al.*, Recent intensification of winter haze in China linked to foreign emissions and meteorology. *Sci. Rep.* **8**, 2107 (2018).
55. S. Kobayashi *et al.*, The JRA-55 reanalysis: General specifications and basic characteristics. *J. Meteorol. Soc. Jpn.* **93**, 5–48 (2015).
56. D. P. Dee *et al.*, The ERA-Interim reanalysis: Configuration and performance of the data assimilation system. *Q. J. R. Meteorol. Soc.* **137**, 553–597 (2011).
57. M. G. Bosilovich *et al.*, "MERRA-2: Initial evaluation of the climate" (NASA Tech. Rep. NASA/TM-2015-104606, NASA Goddard Space Flight Center, Greenbelt, MD, 2015). <https://gmao.gsfc.nasa.gov/pubs/docs/Bosilovich803.pdf>. Accessed 22 October 2019.
58. G. J. Huffman *et al.*, The global precipitation climatology project (GPCP) combined precipitation dataset. *Bull. Am. Meteorol. Soc.* **78**, 5–20 (1997).
59. R. F. Adler *et al.*, The version 2 global precipitation climatology project (GPCP) monthly precipitation analysis (1979-present). *J. Hydrometeorol.* **4**, 1147–1167 (2003).
60. J. Key, X. Wang, Y. Liu, R. Dworak, A. Letterly, The AVHRR polar pathfinder climate data records. *Remote Sens.* **8**, 167 (2016).
61. K. G. Karlsson *et al.*, CLARA-A2: The second edition of the CM SAF cloud and radiation data record from 34 years of global AVHRR data. *Atmos. Chem. Phys.* **17**, 5809–5828 (2017).
62. M. M. Holland, D. A. Bailey, B. P. Briegleb, B. Light, E. Hunke, Improved sea ice shortwave radiation physics in CCSM4: The impact of melt ponds and aerosols on Arctic Sea Ice. *J. Clim.* **25**, 1413–1430 (2012).
63. M. G. Flanner, K. M. Shell, M. Barlage, D. K. Perovich, M. A. Tschudi, Radiative forcing and albedo feedback from the Northern Hemisphere cryosphere between 1979 and 2008. *Nat. Geosci.* **4**, 151–155 (2011).